Reaction Chemistry & Engineering

ROYAL SOCIETY OF CHEMISTRY

PAPER

View Article Online
View Journal | View Issue

Check for updates

Cite this: *React. Chem. Eng.*, 2025, 10, 894

Flat-plate mesophotoreactor with a serpentine channel and inclined baffles for balancing mixing performance and reaction throughput†

Shuaiyu Chen,‡[a] Qianrui Lv, ‡[b] Fujun Li,[a] Yuchao Wang, [a] Wenbo Yang, [a] Zhimei Liu,[d] Alexander A. Miskevich,[c] Valery A. Loiko,[c] Shengyang Tao [a] and Lijing Zhang *[a]

This study aims to address the main challenges encountered during the scale-up of flat-plate microreactors in photochemical processes: the decline in mixing and mass transfer efficiency, and the decrease in light energy utilization. Although microreactors have been widely studied for their efficient mass transfer and light energy utilization, the degradation of their performance during scale-up has limited their application in industrial production. Here, a strategy was explored to enhance the mixing efficiency by introducing inclined baffle structures within the mesoscale channel. The performances of a conventional 1 mm microreactor and an optimized mesoreactor with baffles were compared in the homogeneous photochemical reaction. The results indicated that under similar residence times, the yields of both reactors were nearly the same, but the reaction flux was increased by about 180 times compared to the microreactor. The characteristic mixing time (t_m) and the second Damköhler number (Da_{II}) for the mesoscopic reactor with baffles were similar to those of the microreactor. This result demonstrates the validity of the scale-up strategy in maintaining high mixing and mass transfer efficiency. The performance of the mesoreactor with baffles in heterogeneous reactions was also investigated, and high yields were achieved by extending the length of the reactor channel. The photochemical space time yield (PSTY) of the baffled mesoreactor with extended channels almost doubles that of the microreactor. This study provides an effective method for scaling up plate-type photochemical microreactors, opening up new possibilities for the application of microreactors in industrial production.

Received 29th October 2024,
Accepted 3rd January 2025

DOI: 10.1039/d4re00523f

rsc.li/reaction-engineering

1. Introduction

During the photochemical reaction process, light energy transfer and mass transport within the reactor space are two crucial factors that restrict the efficiency of the photochemical reaction.[1–3] The emergence of photochemical microreactors offers a new strategy to improve the photoreaction conversion rate. Compared to conventional batch photoreactors, microchannels of small size (<1 mm) are characterized by high mass and heat transfer efficiency, high mixing efficiency, uniform illumination throughout the system, and a high utilization rate of light energy, which are considered as a highly efficient solution for photochemistry.[4–7] They have been widely used in the synthesis of high-value chemical products due to these advantages, such as in the synthesis of pharmaceuticals and pesticides.[8,9] Nevertheless, like other microreactors, the throughput of a single reactor is limited due to the size and flow rate constraints.[10,11] In addition, the distribution of light in the microreactor should be taken into account. This depends on many factors. Such as the characteristic size and structure of the reactor. When there is a particulate medium within the reactor channels, factors such as its concentration, absorption, and scattering effects should also be considered.[12–14] According to the Bouguer–Lambert–Beer law, the intensity of light rapidly attenuates as the characteristic dimensions of the reactor increase.[15,16] Therefore, to meet the practical demands of industrial production, researching reactor scale-up is a significant challenge currently.[17]

Nowadays, many researchers use different scale-up methods to enhance the flux of microreactors, such as

[a] School of Chemistry, State Key Laboratory of Fine Chemicals, Frontier Science Center for Smart Materials, Dalian Key Laboratory of Intelligent Chemistry, Dalian University of Technology, Dalian 116024, China. E-mail: zhanglj@dlut.edu.cn
[b] School of Physical Science and Engineering, Beijing Jiaotong University, Beijing 100044, China
[c] Institute of Physics, National Academy of Sciences of Belarus, 68-2 Niezalezhnastsi ave., Minsk, 220072, Belarus
[d] QinHuangDao Administration for Market Regulation, QinHuangDao 066000, China
† Electronic supplementary information (ESI) available. See DOI: https://doi.org/10.1039/d4re00523f
‡ Co-first authors.

extending the channel length and increasing the number of channels. However, these methods do not essentially change the micrometer scale of the microreactor, and thus the enhancement of the reaction flux is very limited.[9] Mesoreactors have gained a lot of attention, which are mesoscale reactors with characteristic dimensions in the millimeter range.[18–21] They can be regarded as the size enlargement of microreactors, offering distinct advantages in terms of throughput expansion and blockage prevention. However, the mixing and mass transfer processes within microchannels are dominated by molecular diffusion[22–24] directly enlarging the size of a microreactor will undoubtedly weaken the intermolecular diffusion, leading to a decrease in the mixing and mass transfer efficiency.[25,26] Consequently, compared to microreactors, mesoreactors have limited mixing and mass transfer efficiency. For photochemical reactions, the weakness of mesoreactors is even more pronounced. According to the Grotthuss–Draper law, light must be absorbed by chemical substances for a photochemical reaction to take place, whereas insufficient mixing will result in certain reactants staying inside the darkness, deprived of the opportunity to be fully irradiated by light, thus failing to react completely.[27,28] Therefore, it is more significant to solve the problem of mixing efficiency in mesoscopic photoreactors, not only to increase the collision chances of reacting molecules, but also to create conditions for light to be absorbed by more reactants.

Introducing special geometric structures within the reactor channels can effectively address the issue of mixing and mass transfer.[29] Zhao *et al.*[30,31] enlarged the microchannel dimension from 1 mm to 10 mm and then introduced elliptical obstacles into it, resulting in a maximum increase of 65% in the mixing index and was comparable to that of a microreactor. Santana *et al.*[32] introduced a baffle structure into a serpentine channel with a width of 1.5 mm. The ester exchange reaction between sunflower oil and ethanol demonstrated that the reactor with baffles exhibited superior performance in mixing efficiency and reaction conversion. After the introduction of baffles in the reactor channel, the reaction conversion rate increased from 58.2% to 76.6%. In terms of enhancing light energy utilization, Wang *et al.*[33] designed a novel photobioreactor by introducing baffles into centimeter-scale rectangular channels. The baffle parameters were optimized through fluid dynamics. Experimental results showed that compared to the reactor without baffles, the optimized reactor achieved a 45.7% increase in the maximum algal biomass. The research group led by Cheng[34,35] added butterfly-shaped and Tesla-valve baffles to the channels of a dual-column photobioreactor, respectively. The optimized reactors effectively reduced the mixing time and increased the biomass compared to the reactors without baffles. The studies above demonstrate that constructing geometric structures within reactor channels can significantly reduce mixing time and enhance mass transfer efficiency as well as light energy utilization. A flat-plate photoreactor has a higher light exposure area compared to a tubular photoreactor, and its light distribution is more uniform,[36] thereby exhibiting better performance and application potential in photoreactions. However, there is currently limited research on flat-plate mesoscopic photoreactors, and the scale-up of photoreactors primarily focuses on capillary reactors. For instance, Sheng *et al.*[25] used the photochemical synthesis of a steroid intermediate as a model reaction after the capillary diameter was enlarged from 0.6 mm to 4 mm; convective mixing was promoted by introducing microbubbles into the channel, thereby improving the reaction efficiency. Compared to a 4 mm channel without microbubbles, the reaction yield increased by 70%, and the side products decreased by 86%. Despite the significant advantages of plate photoreactors in terms of photoreactivity, research on them is rather insufficient. In particular, the ability and mechanism of baffles to enhance mass transfer and facilitate light energy utilization are unclear and need to be further explored.

Herein, a novel reactor design is presented, featuring inclined baffle structures constructed within the curved channel of a flat-plate serpentine photochemical mesoreactor to strengthen mixing efficiently, enabling it to achieve size scale-up while still taking into account the high mixing and mass transfer efficiency as well as high light utilization of the microreactor. Numerical simulations were used to optimize the structural parameters and placement of the baffle in detail, and the reasons why the introduction of baffle structures can enhance mixing and mass transfer were discussed based on Dean vortex theory. The optimized microreactor channel size was scaled up to 5 mm (width) × 3 mm (height). Subsequently, the reactors were fabricated using glass thermal bonding, and the enhanced mixing effect of the reactor with baffles was verified through an ink mixing experiment. Heterogeneous mixing simulations were also conducted for different mesoreactors to investigate their mixing behaviour in two phases. The performance of the mesoreactor with baffles was evaluated by both homogeneous and heterogeneous photochemical reactions, and the validity of the scale-up of the microreactor, as well as the practicality of the mesoreactor with baffles, was confirmed by comparing the characteristic mixing time (t_m value) and the second Damköhler number (Da_{II} value) of the different reactors. Finally, the advantage of the high output of the baffled mesoreactor with an extended channel length over the microreactor was demonstrated by calculating the photochemical space time yield (PSTY). The mesoreactor with baffles designed in the paper shows great potential in the industrial production of pharmaceuticals and pesticide intermediates.

2. Materials and methods

2.1. Modeling and boundary conditions

The reactor and baffle parameters were optimized using COMSOL Multiphysics simulation software. To compare

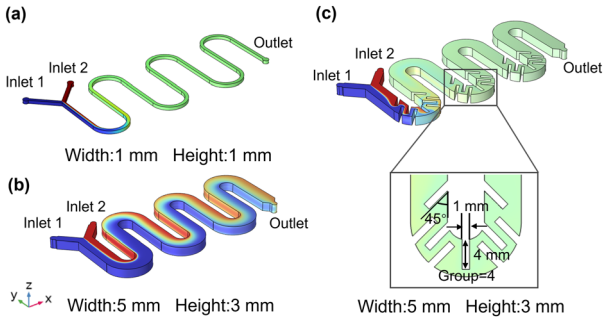

Fig. 1 Geometric schematics of the (a) microreactor ($\mathbf{M_1}$), (b) the mesoreactor without baffles ($\mathbf{M_2}$), and (c) the optimized baffled mesoreactor ($\mathbf{M_3}$).

with the microchannel reactor, a reactor ($\mathbf{M_1}$) was first established with a channel width and height of 1 mm each, as shown in Fig. 1a. Subsequently, the size of $\mathbf{M_1}$ was scaled up, and the geometries of the mesoreactor without baffles ($\mathbf{M_2}$) and the optimized baffled mesoreactor ($\mathbf{M_3}$) are shown schematically in Fig. 1b and c, respectively. Both reactors have a channel width of 5 mm and a reactor height of 3 mm. The optimized mesoreactor has 4 groups of baffles placed within the curved channel; each baffle has a length of 4 mm, a width of 1 mm, and an angle of 45°. The specific optimization process is illustrated in Fig. S1–S3 (ESI†). The reactors are equipped with two inlets and one outlet. During the simulation, the concentration at inlet 1 is set to 0, while the concentration at inlet 2 is set to 1000 mol m^{-3}. The boundary conditions at the inlet and outlet are laminar inflow and outflow, respectively. A no-slip boundary condition is applied at the inner wall of the channel and a zero-pressure boundary condition is specified at the outlet. The diffusion coefficient is 1×10^{-9} m^2 s^{-1}.

2.2. Governing equations

The laminar flow and transport of the diluted species' physical fields are used to solve the fluid mixing phenomena in reactor channels. The flow field is obtained by solving the Navier–Stokes equations for an incompressible Newtonian fluid under steady-state pressure-driven conditions:

$$\left[\frac{\partial \boldsymbol{u}}{\partial t} + (\boldsymbol{u}\cdot\nabla)\boldsymbol{u}\right] = -\nabla p + \eta\nabla\boldsymbol{u} \quad (1)$$

$$\nabla\cdot\boldsymbol{u} = 0 \quad (2)$$

where $\boldsymbol{u}$ is the velocity vector, ρ is the density of the fluid, t is the time, η is the dynamic viscosity, and p is the pressure. Eqn (1) and (2) represent the equation of momentum balance and continuity for incompressible fluids, respectively. The convective diffusion equation (eqn (3)) is used for calculating the substance concentration throughout the reactor:

$$\frac{\partial c}{\partial t} = D\nabla^2 c - \boldsymbol{u}\cdot\nabla c \quad (3)$$

where c is the concentration, D is the diffusion coefficient, and $\boldsymbol{u}$ is the velocity vector.

2.3. The fabrication of reactors

To ensure the transmittance of the photoreactor, a glass material was selected to fabricate the reactors. The reactors were obtained by the method of thermal bonding. Each reactor consists of three layers of glass, where the first layer is equipped with three small holes corresponding to the two inlets and one outlet of the reactor for liquid inflow and outflow, the second layer is the serpentine perforated channel of our design, and the bottom layer is the base glass. After the above glass pieces are cleaned, they will be immersed in piranha solution for 2 h, ultrasonically cleaned, vacuum dried for 12 h, and gradient heated to 600 °C for 4 h in a muffle furnace. After these operations, the reactors will be obtained. Fig. 2a–c show the actual reactors of $\mathbf{M_1}$, $\mathbf{M_2}$, and $\mathbf{M_3}$, respectively.

2.4. Evaluation of mixing effects

The mixing effects within the reactor channels are quantified by calculating the mixing index, which is obtained by extracting and calculating the variance of all concentration points at the selected space.[37–40] The calculation formula is as follows:

$$\mathrm{MI} = \left(1 - \sqrt{\frac{\sigma^2}{\sigma^2_{\max}}}\right) \quad (4)$$

where $\sigma^2_{\max}$ is the maximum variance of component concentrations (inlet) and σ^2 is the variance of different positions. MI is between 0 and 1; the closer to 1, the better the mixing effect. Fluid flow is primarily driven by pressure gradients. In the case of high-pressure drop, a greater driving force is required, which leads to higher energy consumption. Therefore, when evaluating the overall performance of a reactor, the pressure drop must be considered together with the mixing index.[31,41] The calculation formula for the pressure drop is as follows:

$$\Delta P = P_i - P_o \quad (5)$$

where P_i is the pressure of the inlet and P_o is the pressure of the outlet.

2.5. Grid independence test

The calculation results are significantly affected by the choice of the number of grids in the simulation process.

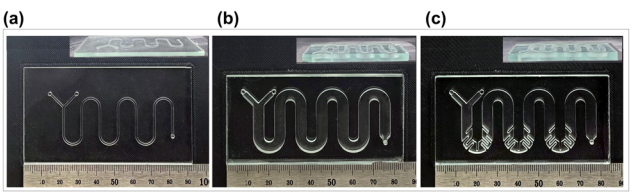

Fig. 2 Actual reactor photographs of (a) $\mathbf{M_1}$, (b) $\mathbf{M_2}$, and (c) $\mathbf{M_3}$.

The more grids are selected, the more truly the fluid flow and mixing situation in the reactor channel can be represented, but the computational time will also be greatly increased. To ensure that the simulation results are independent of the grid size, it is necessary to select a reasonable grid size for the fluid domain. We intend to use the mixing index at the specific locations of the reactor as an evaluation parameter to determine the optimal number of grids for simulation calculation.

2.6. Ink mixing experiment

First, 100 μL red ink was dissolved in 50 mL deionized water to prepare a red ink solution as the storage solution. Subsequently, the red ink solution and deionized water were separately pumped into the reactor from inlet 1 and inlet 2 at the same flow rate and underwent mixing. Finally, the mixing effects of the three reactors were obtained by taking the mixing images in the reactor channels under the same experimental conditions.

2.7. Homogeneous photochemical reaction

The photochemical reaction 1,5-dihydroxy naphthalene (DHN) oxidation experiment was chosen as a model reaction. The stock solutions of DHN (250 mL solution of 0.25 mM in ACN) and 2I-BDP (250 mL solution of 0.04 mM in ACN) were prepared. The photosensitizer 2I-BDP is a molecule synthesized in our laboratory.[42] Both solutions must be stored strictly away from light. Before the reaction, oxygen was bubbled into the acetonitrile solution of photosensitizer 2I-BDP for 1 h to ensure oxygen saturation. The light source used in the reaction is an LED with an emission wavelength of 505 nm. The surface light power density of the reactor can be measured with a light power density meter (CEL-NP2000), and the residence time can be achieved by adjusting the injection pump flow rate. To ensure that the photochemical reaction only takes place within the reactor, the syringe and the inlet and outlet capillaries need to be wrapped with tin foil. The outlet liquid is collected through a 5 mL centrifuge tube (wrapped in tin foil) and then the absorbance at 403 nm (the optimal absorption peak for juglone) is measured using a UV-visible spectrophotometer (TU-1900 double beam UV-vis) to calculate the reaction yield.

2.8. The simulations of heterogeneous mixing

A two-dimensional transient multiphase computational fluid dynamics model was established using laminar flow and level set physics fields to simulate the mixing behavior of two-phase fluids within the reactor channel. The two-phase fluids are water and 1,2-dichloroethane, respectively. The flow field characteristics and flow behavior within the reactor channel can be qualitatively assessed through the color distribution. The governing equations for the laminar flow physics field are the same as those in section 2.2 and the governing equation for the level set physics field is as follows:

$$\frac{\partial \phi}{\partial t} + \boldsymbol{u}\cdot\nabla\phi = \gamma\nabla\cdot\left[-\phi(1-\phi)\frac{\nabla\phi}{|\nabla\phi|} + \varepsilon\nabla\phi\right] \quad (6)$$

where ρ is the density of the fluid, $\boldsymbol{u}$ is the velocity vector, t is the time, p is the pressure, ϕ is the level set function, and γ and ε are the numerical stability parameters.

2.9. Heterogeneous photochemical reaction

The photo-bromination reaction of methyl 2-(methoxyimino)-2-*o*-tolylacetate (MMOT) was chosen as the model reaction to investigate the performance of $\mathbf{M_2}$ and $\mathbf{M_3}$ in a heterogeneous photochemical reaction. The specific experimental operations are as follows: reaction solutions 1 and 2 were 9.79 mol L^{-1} hydrogen peroxide solution and 8.8 mol L^{-1} hydrogen bromide solution, respectively; reaction solution 3 was 0.6 mol L^{-1} MMOT solution, and the solvent was 1,2-dichloroethane; and 0.6 mol L^{-1} aqueous sodium thiosulfate solution was used as the terminator of the reaction. First, reaction solutions 1 and 2 were transported by an injection pump to a T-shaped mixer and then entered a 3 mL capillary microreactor to generate liquid bromine (aqueous phase). Subsequently, the liquid bromine and 0.6 mol L^{-1} solution of MMOT (oil phase) caused photochemical reactions in $\mathbf{M_2}$ and $\mathbf{M_3}$. The light source is an LED with an emission wavelength of 405 nm, the surface light power density of the reactor is 200 mW cm^{-2}, and the water bath temperature is 45 °C. After the system was stabilized, a centrifuge tube containing sodium thiosulphate solution was used to collect the reaction solution. After thorough shaking and allowing the solution to static layering, multiple extractions were performed to clarify the upper aqueous phase to transparency. Then, the aqueous phase was removed and dried with anhydrous sodium sulfate. The reaction yield was measured using HPLC (Agilent 1260).

3. Results and discussion

3.1. Grid independence test

In fluid dynamics problems, the inclusion of a boundary layer mesh is favorable for improving the accuracy of calculations near the walls. Hence, a boundary layer mesh at the model boundary was set up to ensure a reasonable transition with the domain body mesh to prevent the generation of deformed meshes. The three magnified areas correspond to the mesh distribution of the body mesh, the boundary layer and the baffle edges, respectively (Fig. 3a). The difference in the mixing index caused by the number of grids is shown in Fig. 3b, and the simulated inlet flow rate is 0.5 mL min^{-1}. The three lines in Fig. 3b correspond to the position of $\mathbf{M_3}$ after passing through the baffle structures of groups 1, 2, and 3, respectively. For grids numbered 1–5 shown in Fig. 3, the number of grids is 5.5×10^5, 1.4×10^6, 4.0×10^6, 1.8×10^7 and 2.1×10^7, respectively. As the number of grids increases (Fig. 3b), the decline in the mixing index at **positions B** and **C** is not obvious, with the overall variation kept within 10%. The mixing index at **position A** exhibits a

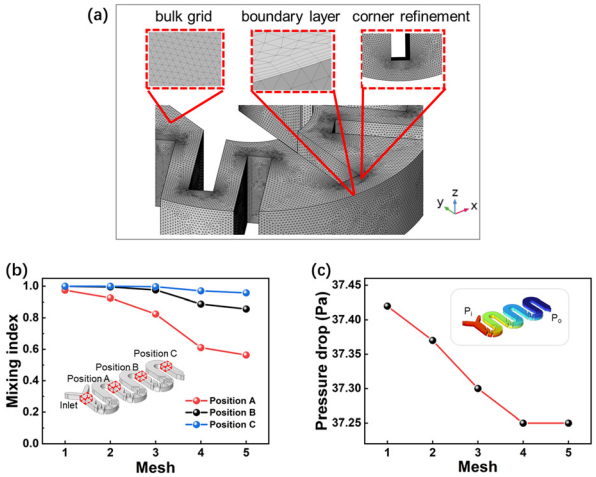

Fig. 3 (a) Schematic diagram of the model grids. (b) The variation of the mixing index at **positions A**, **B**, and **C** of M_3 with the number of grids. (c) The fluctuation of pressure drop at the inlet and outlet of M_3 with the number of grids.

more pronounced decrease with the increase in the number of grids; in particular, the number of grids increases from 3 to 4, resulting in a 20% decline at **position A**. However, when the number of grids further rises from 4 (1.81×10^7) to 5 (2.12×10^7), the decrease in the mixing index at **position A** is only 5%, the data fluctuates within 10%, and the mixing index gradually stabilizes. Fig. 3c illustrates the variation of the overall pressure drop in a reactor with the number of grids. As the grid count increases, there is a continuous decrease in pressure drop. And when the number of grids increases from 4 to 5, the pressure drop remains unchanged. Considering that mesh refinement leads to a sharp increase in the computational time and cost of the model, depending on the fluctuation of the mixing index and pressure drop, grid 4 (1.81×10^7) was selected for subsequent simulations.

3.2. Optimization of baffle positions and comparison of mixing effects before and after reactor scale-up

When fluid flows through a curved channel, the fluid at the center flows faster than the fluid around it. The central fluid is driven outward by a stronger centrifugal force, while the external fluid is pushed towards the top and bottom. As a result, a pair of counter-rotating vortices, known as Dean vortices, are formed. The chaotic advection caused by Dean vortices is one of the most effective ways for fluid mixing.[43–45] Therefore, the placement influence of the baffles on the velocity field at different cross-sections of the reactor was first discussed. Fig. 4a, from left to right, shows the velocity streamline diagrams of the *YZ* cross-section of the serpentine reactor with no baffle added (M_2), baffles placed at the curved channel (M_3), and with baffles placed at the straight channel (M_4), respectively (with an inlet flow rate of 2 mL min^{-1}). It can be observed that Dean vortices appear in all three types of reactors as the fluid flows through them. The maximum velocity of the vortices in the *YZ* cross-section of the M_3 and M_4 reactors is significantly higher than that of the M_2 reactor. Compared to M_4, the center of the Dean vortices in M_3 shifts to the left, which may be due to the different flow patterns when the fluid passes through the vertical baffles. Subsequently, the velocity streamline diagrams of the *XY* cross-section for different reactors were compared (Fig. 4b). Compared to M_2, for both M_3 and M_4, at a flow rate of 0.5 mL min^{-1}, the baffles acting as obstacles that bend the fluid may be beneficial for improving mixing efficiency; at a flow rate of 2 mL min^{-1}, smaller vortices are formed near the baffle channel; and when the flow rate is increased to 5 mL min^{-1}, significantly larger vortices appear within the channels. The two points above indicate that the reinforcement of Dean vortices and vortex generation can be achieved by introducing a baffle structure within the serpentine channel, which theoretically will intensify the

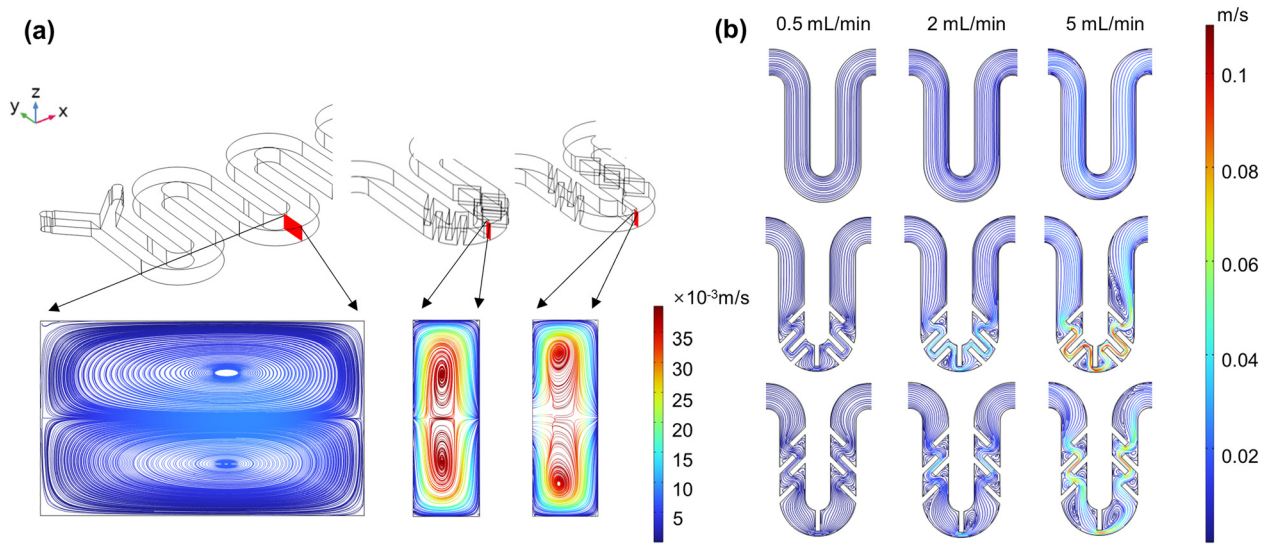

Fig. 4 Velocity streamline diagrams at different cross-sections for M_2–M_4: (a) *YZ* cross-section and (b) *XY* cross-section.

collision of fluids within the channel, thereby enhancing the mixing effect.

To verify this idea, a simulation analysis of the mixing effects of $\mathbf{M_2}$, $\mathbf{M_3}$, and $\mathbf{M_4}$ was conducted. The selected flow rate range was 0.01–10 mL min^{-1}, and all concentration points at **positions A** and **C** were extracted to calculate the mixing index according to eqn (4) (Fig. 5a and b). At **position A**, the mixing index of all three reactors shows a trend of decreasing first and then increasing as the flow rate increases. The inflection points for $\mathbf{M_2}$–$\mathbf{M_4}$ all appear at 0.5 mL min^{-1}. Throughout the entire range of flow rates, the mixing index of $\mathbf{M_3}$ is significantly better than that of $\mathbf{M_2}$ (>25%). Compared to $\mathbf{M_3}$, $\mathbf{M_4}$'s overall mixing effect is not as good, except when the flow rate is at 0.01 mL min^{-1} and above 3 mL min^{-1}. When the flow rate was 0.5 mL min^{-1}, the mixing index $\mathbf{M_3}$ was about 16% higher than that of $\mathbf{M_4}$. At the reactor outlet (Fig. 5b, **position C**), $\mathbf{M_3}$ achieves complete mixing throughout the entire range of flow rates studied. $\mathbf{M_4}$ experiences a decrease in the mixing index within the flow rate range of 0.025–1 mL min^{-1}, while $\mathbf{M_2}$ shows an obvious decrease in the mixing index within the flow rate range of 0.025–5 mL min^{-1}. It is clear that $\mathbf{M_2}$ loses its ability to work within this flow range, and it only exhibits good mixing effects at flow rates of 0.01 mL min^{-1} and 10 mL min^{-1}. This is respectively due to the dominance of intermolecular diffusion (viscous forces) and chaotic advection (inertial forces).[46–49] This indicates that the convective diffusion mechanism still exists in the size scale-up mesoreactor channel, and this mechanism is most effectively enhanced by the addition of baffles at the curved channels of the serpentine reactor ($\mathbf{M_3}$), particularly within the flow rate range of 2–10 mL min^{-1}, where there is a significant improvement in mixing efficiency. The introduction of baffles in the serpentine curved channels promotes mixing more effectively because there is a larger velocity gradient as the fluid flows through the curved channels compared to a straight channel, subjecting the fluid to greater shear to enhance mixing, and the fluid is subjected to centrifugal forces which help to increase the perturbation of the fluid to create secondary flows (Dean vortices) and the addition of baffles creates more enhanced vortices, which in turn enhances the mixing of the fluid internally.[50,51] In addition, the path of the fluid in the curved channel is longer compared to the straight channel, providing more time for mixing. Therefore, while adding baffles to the serpentine straight channels can enhance mixing to some extent, this method does not fully utilize the advantages of the serpentine structure. However, adding baffles to the curved channels combines the advantages of both, effectively intensifying the mixing effect. After optimizing the baffle's position, a comparison of the mixing effects between $\mathbf{M_1}$ and $\mathbf{M_3}$ was conducted (Fig. 5a and b). At **position A**, when the flow rate exceeds 2 mL min^{-1}, $\mathbf{M_3}$ achieves a mixing index comparable to $\mathbf{M_1}$, nearing complete mixing. At **position C** (the outlet), throughout the entire range of flow rates studied, both $\mathbf{M_3}$ and $\mathbf{M_1}$ achieve complete mixing. This demonstrates that the reactor with baffles added to the curved channels of the serpentine mesoreactor is more similar to the microreactors in mixing effects, verifying the feasibility of the reactor scale-up idea.

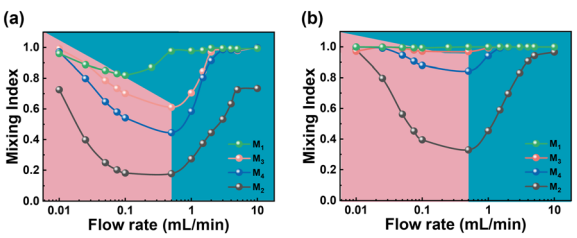

Fig. 5 Mixing effect of different reactors: (a) **position A** and (b) **position C**.

3.3. Comparison of experimental results with simulation

Fig. 6 exhibits concentration distribution images obtained through simulation and experimental results for $\mathbf{M_1}$, $\mathbf{M_2}$, and $\mathbf{M_3}$ at different flow rates. It can be observed that $\mathbf{M_1}$ shows excellent mixing effects within the selected flow range (Fig. 6d), which is in close agreement with the simulation results (Fig. 6a). However, when the size of $\mathbf{M_1}$ is scaled up to $\mathbf{M_2}$, it is evident from Fig. 6b and e that the mixing efficiency of $\mathbf{M_2}$ drastically decreases. Except for the flow rate of 5 mL min^{-1}, where near complete mixing is achieved at the outlet, full mixing is not attained at the remaining flow rates. For $\mathbf{M_3}$, as the flow rate increases from 0.1 mL min^{-1} to 0.5 mL min^{-1}, the mixing efficiency at **position A** becomes worse. However, as the flow rate further increases to 2 mL min^{-1} and then to 5 mL min^{-1}, the mixing efficiency significantly improves (Fig. 6c and f), with the mixing distance noticeably shortening, reaching a level comparable to that of $\mathbf{M_1}$. This is in line with the pattern of mixing index variation with the flow rate obtained through simulation in section 3.2., verifying the reliability of the simulation results. This also indicates that the model has good precision and can predict the concentration distribution after fluid mixing more accurately.

3.4. Experimental results of the homogeneous photochemical reaction

Fig. 7 illustrates the schematic diagram of the homogeneous photochemical reaction. DHN solution and 2I-BDP solution enter the reactor from inlets 1 and 2 at the same flow rate and undergo a photochemical reaction. The experimental results are shown in Fig. 8. As can be seen from Fig. 8a, the residence time is the most critical factor affecting the reaction yield when the flow rate is less than 0.5 mL min^{-1}; consequently, the difference in the reactor structure is not obvious. However, when the flow rate exceeds 0.5 mL min^{-1}, the reaction yield of $\mathbf{M_3}$ is significantly higher than that of $\mathbf{M_2}$, which indicates that the addition of baffles at this point is extremely favorable for the enhancement of the efficiency of the photochemical reaction. This is largely due to the improvement in mixing efficiency. The effect of $\mathbf{M_1}$ on the

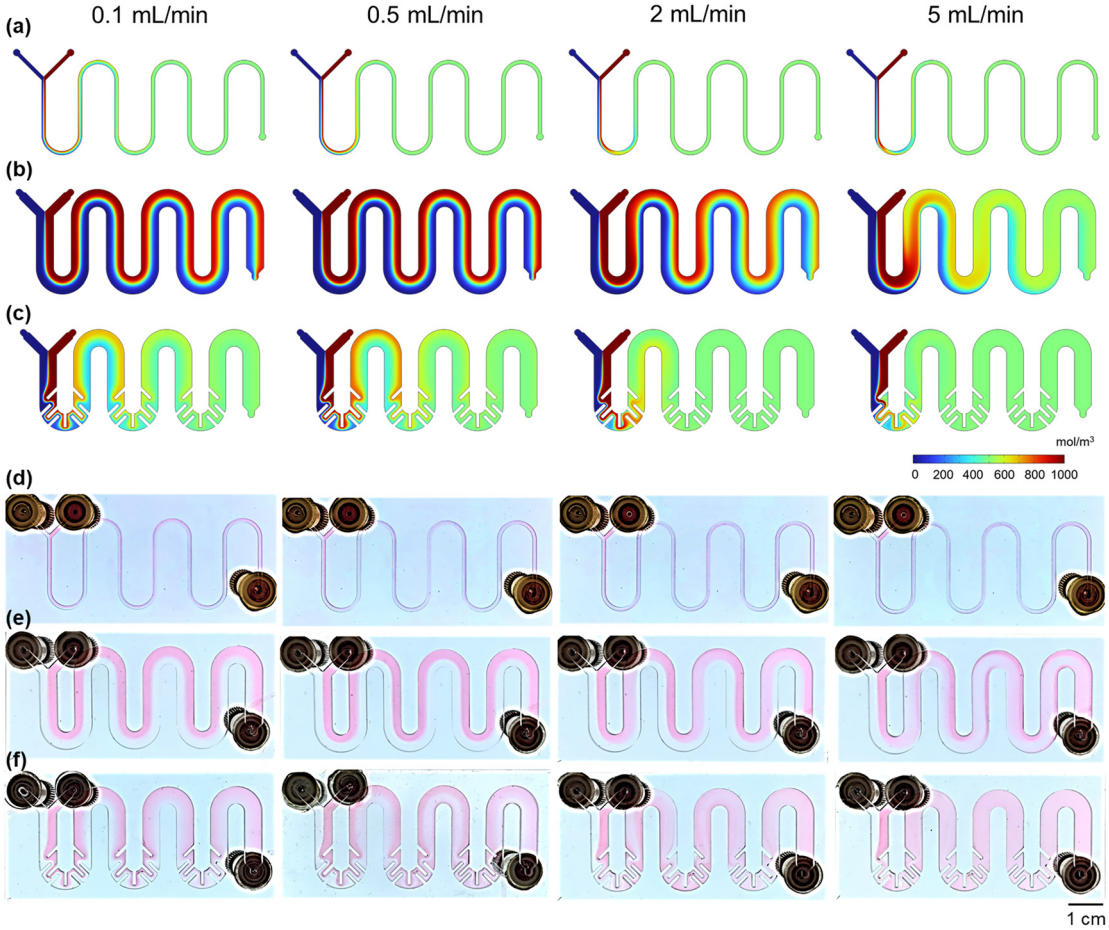

Fig. 6 Simulation results for (a) M_1, (b) M_2, and (c) M_3 and experimental results for (d) M_1, (e) M_2, and (f) M_3.

reaction was then evaluated. A comparison of Fig. 8a and d reveals that at a flow rate of 1 mL min^{-1}, M_3 exhibits a 77.8% higher yield than M_1; at a flow rate of 3 mL min^{-1}, the yield of M_3 is 1.5 times higher than that of M_2, demonstrating the advantage of M_3 at the same flow rates.

To investigate the effect of light power density on the reaction performance, the yields of the three reactors were compared after increasing the light power density (Fig. 8b–d). The results showed that the yields of all three reactors were improved overall, but M_3 still exhibited the best reaction performance at high flow rates. To highlight the advantage of baffles in enhancing reaction performance, the yield improvement rates of M_3 relative to M_2 were compared under different light power densities (Fig. 8e). It can be seen that as the light power density decreased, the yield improvement rates increased significantly. This is because as the light intensity weakens, the distance that light can travel through the solution decreases. At this point, mixing plays a key role in the reaction effect by allowing the fluid in the dark zones to be turned over to the light-irradiated areas to absorb photons, thus effectively boosting the utilization of light energy and consequently improving the reaction efficiency. In addition, the yields of M_1 (0.25 mL min^{-1}), M_2 (3 mL min^{-1}) and M_3 (3 mL min^{-1}) under conditions where the residence time was similar were compared. From Fig. 8f, it can be observed that M_3 significantly outperforms M_2 in terms of reaction efficiency and is comparable with M_1. However, under the condition of equal yields, reactor M_3 increases the volume by about 15 times and the flow rate by 12 times compared to M_1, thus increasing the reaction flux by about 180 times. The analysis above proves that adding baffle structures into mesoscopic photochemical reactor channels is an effective means of enhancing light energy utilization and intensifying mixing and mass transfer efficiency, which is comparable to the effect of a microreactor. Finally, the channel of M_3 was extended to increase its volume to 9 mL ($M_{3\text{-large}}$) and its reaction performance was evaluated (Fig. S5 in the ESI†).

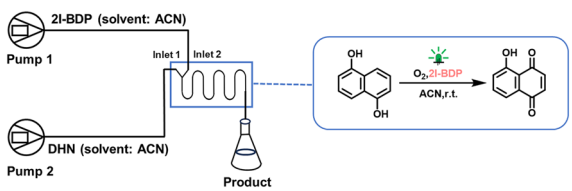

Fig. 7 Schematic diagram of the photo-oxidation reaction.

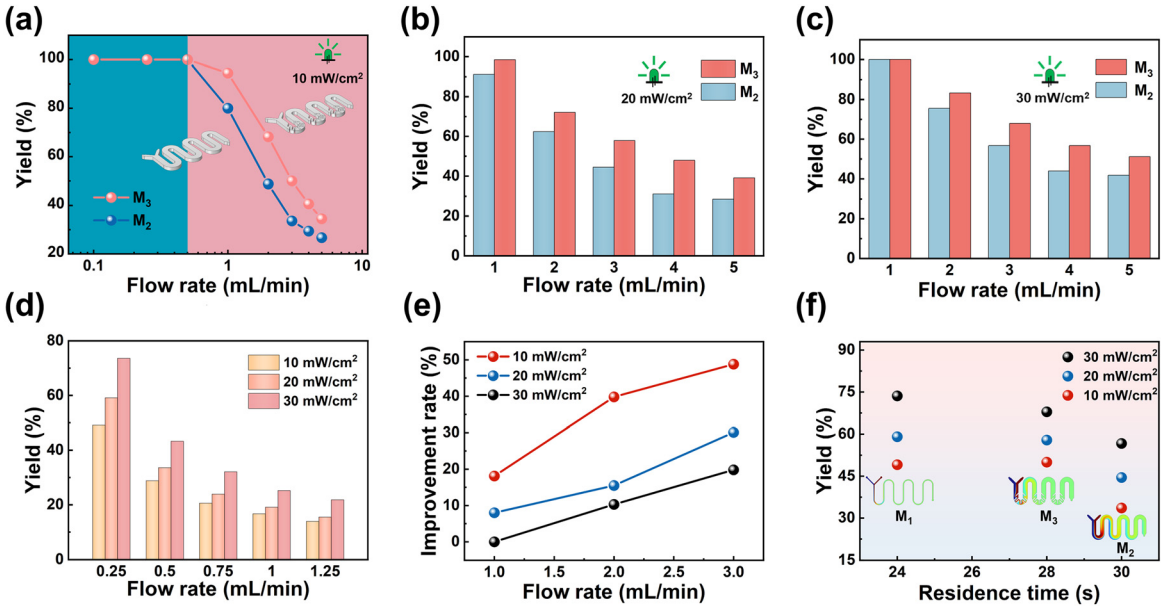

Fig. 8 Variation of juglone yield with the flow rate in different reactors. (a) M_2 and M_3 (10 mW cm^{-2}). (b) M_2 and M_3 (20 mW cm^{-2}). (c) M_2 and M_3 (30 mW cm^{-2}). (d) M_1 (10–30 mW cm^{-2}); (e) comparison of the yield enhancement rates of M_3 under different light power densities. (f) Comparison of the yields of M_1, M_2, and M_3 under different light power densities.

3.5. Assessment of reactor scale-up validity

The characteristic mixing time (t_m) is used to quantitatively evaluate the validity of the photochemical mesoreactor relative to microreactor size scale-up. In channels of different sizes, if the same reaction occurs, the closer the t_m values are, the more similar the reaction conditions will be obtained.[25,52,53] The formula for t_m is as follows:[54,55]

$$t_m = \frac{24.5L^2}{u}\left(\mu \mathrm{Re}^3\right)^{-0.5} \quad (7)$$

where L is the equivalent diameter of the reactor channel (eqn (8)), u is the fluid velocity, μ is the viscosity of acetonitrile, and Re is the Reynolds number, which represents the ratio of inertial force to viscous force.

$$L = \frac{4A}{2(h+w)} \quad (8)$$

where A is the channel cross-sectional area, h is the channel height, and w is the channel width.

$$\mathrm{Re} = \frac{\rho u L}{\mu} \quad (9)$$

The ratio of the reaction rate and the mass transfer rate is represented by the second Damköhler number (Da_{II}). A smaller Da_{II} would be favorable to reduce the negative impact of mass transfer on the reaction.[25] It is calculated as follows:

$$Da_{II} = \frac{t_m}{t_r} \quad (10)$$

where t_r is the characteristic reaction time, and it can be calculated by the following equation:

$$t_r = \frac{1}{k c_0^{n-1}} \quad (11)$$

where k is the intrinsic rate constant, c_0 is the initial concentration of the reactant, and n is the reaction order.

The t_m values of the three types of reactors were calculated using eqn (7) at a flow rate of 3 mL min^{-1}. The t_m value of M_1 is 2.3 × 10^{-5} s, the t_m value of M_2 is 5 × 10^{-2} s and the t_m value of M_3 is 4.4 × 10^{-4} s. It can be found that among the three reactors, M_1 has the smallest t_m value, which is due to its excellent mixing and mass transfer efficiency. However, when M_1 is scaled up to M_2, the t_m value rises steeply, leading to a noticeable decrease in mixing and mass transfer efficiency. Introducing baffles into the M_2 channels results in an obvious decrease in the t_m value, bringing it closer to that of M_1. This indicates that the reaction conditions in M_3 are similar to those in M_1, meaning that after the introduction of baffles, the levels of mixing and mass transfer, as well as the utilization of light energy, are equivalent to those of M_1. For the same reaction occurring in different reactors, the intrinsic rate constant and the reaction order are both the same, which can be considered as constants. Therefore, the order of Da_{II} values for different reactors is completely consistent with the t_m values. This indicates that the negative impact of mass transfer on the reaction occurring in M_1 and M_3 is significantly less than that in M_2. Combining the calculation and analysis of t_m and Da_{II} values for different reactors as discussed above, the validity of the scale-up of the mesoreactor M_3 is proved.

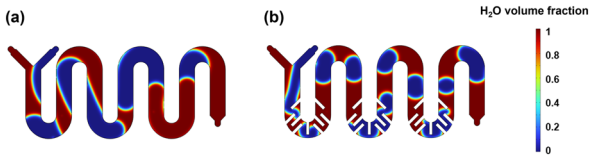

Fig. 9 Heterogeneous mixing simulation results for (a) M_2 and (b) M_3 (the inlet flow rate is 2 mL min^{-1}).

3.6. The results of heterogeneous mixing

Fig. 9 shows red and blue fluids representing water and 1,2-dichloroethane, respectively. The scale indicates the volume fraction distribution of water in the reactor channel, with green representing complete mixing. It can be observed that green appears only at the interface between the two phases. Compared to $\mathbf{M_2}$ (Fig. 9a), the introduction of baffles in the $\mathbf{M_3}$ (Fig. 9b) channel results in a greater shear force being exerted on the fluid as it flows past the baffles. Due to the cutting action of the shear force, the interface between the two phases is dispersed into smaller segments. This effectively increases the contact area between the oil and water phases, promotes the renewal of the oil–water interface, and thereby enhances the mixing effect between the two phases.[56]

3.7. Experimental results of the heterogeneous photochemical reaction

Subsequently, the applicability of $\mathbf{M_3}$ in heterogeneous photochemical reactions was investigated to demonstrate the advantage of $\mathbf{M_3}$ in heterogeneous mixing. This reaction involves two steps: *in situ* bromine generation and photo-bromination, where the mixing process of the aqueous and organic phases is crucial. The experiment explored the bromination yield of MMOT at different flow rates, maintaining a constant molar ratio of liquid bromine to MMOT at 2 : 1 by adjusting the flow rates of injection pumps during the reaction process. Fig. 10 shows the schematic diagram of the heterogeneous photochemical reaction. Fig. 11a displays the yields of bromination reactions using $\mathbf{M_2}$ and $\mathbf{M_3}$, respectively. It is evident that the yield of $\mathbf{M_3}$ is significantly higher than that of $\mathbf{M_2}$, especially at a flow rate of 2 mL min^{-1}, where the yield enhancement rate reaches as high as 228% (as shown in Fig. 11b). This increase is higher than that of the homogeneous reaction (within 50%). This indicates that after scaling up the reactor, introducing baffles into the channels enhances the performance of heterogeneous reactions more notably, confirming their crucial role in intensifying interphase interface mixing and mass transfer. Subsequently, the effect of residence time on the reaction effect at a constant flow rate was explored, and the yields of $\mathbf{M_{3\text{-large}}}$ and $\mathbf{M_{2\text{-large}}}$ (extending the length of the mesoreactor without baffles) were compared. It can be found that $\mathbf{M_{3\text{-large}}}$ still performs better compared with $\mathbf{M_{2\text{-large}}}$, especially when the flow rate is above 3 mL min^{-1} (Fig. 11c). Moreover, extending the $\mathbf{M_3}$ channel to $\mathbf{M_{3\text{-large}}}$ not only boosts the overall yield but also achieves the amplification of the flow rate. At the inlet flow rate of 4 mL min^{-1}, the yield is still maintained at about 50%.

3.8. Comparison of the photochemical space time yield

The space time yield (STY) is commonly used to compare the production capacity of scale-up (non-photo) reactors.[57] The photochemical space time yield (PSTY) is a new benchmark for comparing the production capabilities of different photoreactors, which relates productivity to energy efficiency. Therefore, it is often used to evaluate the feasibility of scaling up the reaction process.[58,59] The calculation formulas for STY and PSTY are shown in eqn (12) and (13), respectively:

$$\mathrm{STY}\left[\mathrm{mol\ m^{-3}\ s^{-1}}\right] = \frac{n\ [\mathrm{mol}]}{V_{\mathrm{reactor}}\ [\mathrm{m^3}]\cdot t\ [\mathrm{s}]} = \frac{c_0\ [\mathrm{mol\ m^{-3}}]\cdot\chi_a}{t\ [\mathrm{s}]} \quad (12)$$

$$\mathrm{PSTY}\left[\mathrm{mol\ kW^{-1}\ day^{-1}}\right] = \frac{86\,400\left[\mathrm{s\ per\ day^{-1}}\right]\mathrm{STY}\left[\mathrm{mol\ m^{-3}\ s^{-1}}\right]}{P\ [\mathrm{kW}]/V_{\mathrm{reactor}}\ [\mathrm{m^3}]} \quad (13)$$

where STY is the space time yield, n is the molar amount of the product, V_{reactor} is the reactor volume, t is the residence time, c_0 is the initial concentration, χ_a is the conversion, PSTY is the photochemical space time yield, and P is the light source power. The PSTY of $\mathbf{M_{3\text{-large}}}$ in the heterogeneous photochemical reaction at a residence time of 2.2 minutes

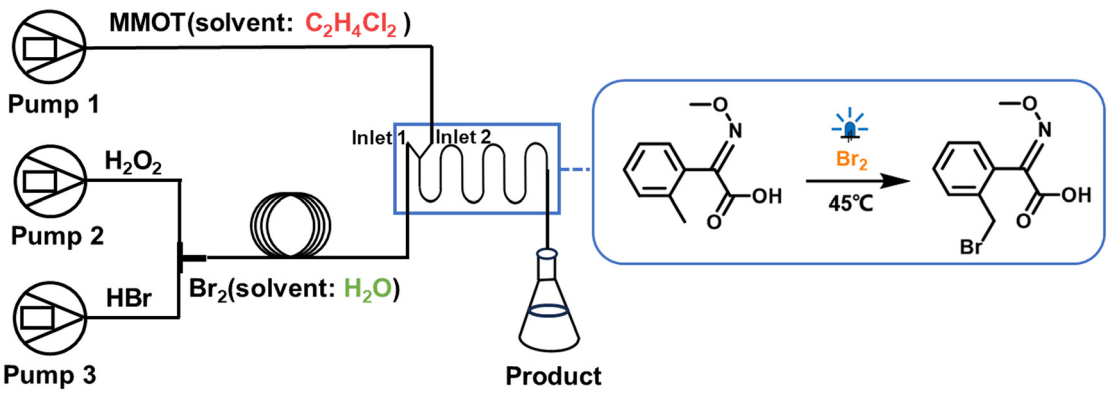

Fig. 10 The schematic diagram of the methyl 2-(methoxyimino)-2-*o*-tolylacetate (MMOT) bromination reaction.

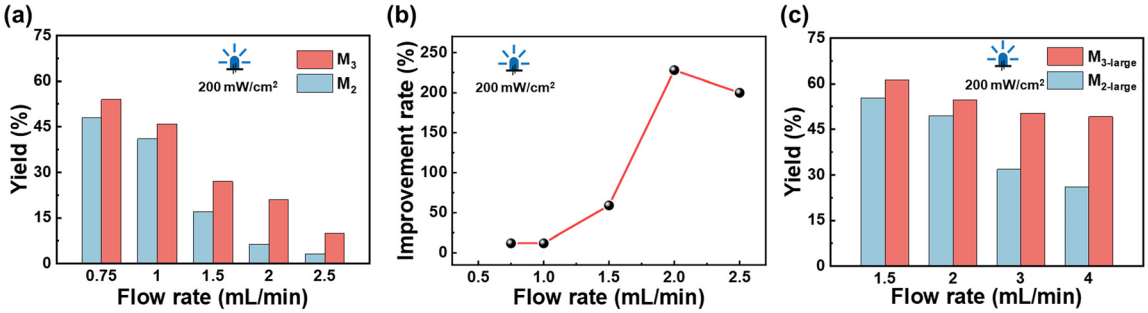

Fig. 11 (a) The yield under the same flow rate in M_2 and M_3. (b) The yield enhancement rate of M_3 at different flow rates. (c) The yield at the same flow rate in $M_{2\text{-large}}$ and $M_{3\text{-large}}$.

(Q_{MMOT} = 3 mL min^{-1}) was calculated using eqn (12) and (13), with a value of 29.96 mol kW^{-1} day^{-1}. In contrast, the PSTY for the same reaction conducted within a capillary microreactor in our group's previous work[60] is 16.81 mol kW^{-1} day^{-1}. This indicates that $\mathbf{M_{3\text{-large}}}$ has a superior production capacity and potential for application in industrial production, demonstrating the effectiveness of reactor scale-up in heterogeneous reactions.

Conclusions

In summary, we have scaled up the microreactors and introduced baffles into the channel, addressing the issue of limited mixing and mass transfer in flat-plate photochemical mesoreactors. Simulation techniques were utilized to optimize the reactor and baffle structure. The reasons why baffles can enhance mixing were analyzed based on the Dean vortex theory. The reliability of the simulations was verified through the ink mixing experiment. In addition, the performance of a traditional 1 mm microreactor and the optimized mesoreactor with baffles were compared in a homogeneous photochemical reaction. Under similar residence times, the yield of $\mathbf{M_3}$ was approximately equal to that of $\mathbf{M_1}$, while the reaction flux was increased by about 180 times. By calculating and comparing the t_m and Da_{II} values of the different reactors, it was found that $\mathbf{M_3}$ has t_m and Da_{II} values similar to those of the microreactor ($\mathbf{M_1}$), confirming the effectiveness of the scale-up strategy used in this study in maintaining high mixing and mass transfer efficiency and high light energy utilization. Additionally, heterogeneous mixing simulations were also conducted for different mesoreactors and their performance in the heterogeneous reaction was investigated and it was found that the mesoreactor with baffles exhibits superior performance, achieving a yield improvement rate of up to 228% at a flow rate of 2 mL min^{-1}. Increasing the reactor channel length can simultaneously enhance both the yield and the production of the reaction to improve the photochemical space time yield. This study provides a new method for the effective scale-up of flat-plate photochemical microreactors and provides important references for further promoting the application of microreactors in industrial production.

Based on the above results, several principles that should be followed when scaling up flat-plate photochemical reactors were summarized as follows: 1. ensure good mixing and mass transfer performance of the reactor. According to the Grotthuss–Draper law, light must be absorbed by chemical substances for a photochemical reaction to take place, whereas insufficient mixing will result in certain reactants staying inside the darkness, deprived of the opportunity to be fully irradiated by light, thus failing to react completely. 2. Ensure good light energy utilization. According to Lambert–Beer's law, light intensity decreases exponentially with the increase in reactor size; therefore, the reactor size must be designed reasonably. 3. Ensure the similarity of mixing time. For the same reaction occurring in channels of different sizes, the closer the mixing time, the more similar the reaction conditions. Therefore, the mixing time of the reactor before and after scaling up should be calculated and compared to determine the validity of the scale-up. The photochemical mesoreactor with baffles designed in this paper adheres to the above principles, making it similar to microreactors in terms of mixing, mass transfer effects, and light energy utilization.

Data availability

The data supporting this article have been included in the ESI.†

Author contributions

Lijing Zhang designed the simulations and experiments; Shuaiyu Chen performed the simulations and experiments and wrote the draft; Fujun Li conducted the product characterization; Qianrui Lv, Yuchao Wang, Wenbo Yang, Zhimei Liu, Yuchao Wang, Alexander A. Miskevich, Valery A. Loiko and Shengyang Tao revised the manuscript. The manuscript was written through the contributions of all authors. All authors have approved the final version of the manuscript.

Conflicts of interest

The authors declare no competing financial interest.

Acknowledgements

The authors acknowledge the financial support from the National Natural Science Foundation of China (No. 22072011, 22272017, 22372025), the Projects of International Cooperation and Exchanges NSFC-BRFFR (No. 22211530456), the Applied Basic Research Programs of Liaoning Province Science and Technology Joint Programme (2023JH2/101700344) Dalian High-Level Talent Innovation Program (No. 2022RQ005), and the Fundamental Research Funds for the Central Universities (DUT24ZD131, DUT22LAB607, 2022JBMC036).

Notes and references

1 J. O. de Brito Lira, H. G. Riella, N. Padoin and C. Soares, *J. Environ. Chem. Eng.*, 2021, **9**(2), 105068.
2 M. Rebber, H. Sannemüller, M. Jaruszewski, D. Pfannkuche, A. Urakawa and D. Koziej, *Chem. Mater.*, 2023, **35**(10), 3849–3858.
3 F. Gaulhofer, M. Metzger, A. Peschl and D. Ziegenbalg, *React. Chem. Eng.*, 2024, **9**(7), 1845–1858.
4 T. M. Masson, S. D. A. Zondag, K. P. L. Kuijpers, D. Cambié, M. G. Debije and T. Noël, *ChemSusChem*, 2021, **14**(24), 5417–5423.
5 F. Mei, H. Lin, L. Hu, W.-T. Dou, H.-B. Yang and L. Xu, *Smart Mol.*, 2023, **1**(1), e20220001.
6 J. Zhang, S. Zhang, C. Peng, Y. Chen, Z. Tang and Q. Wu, *React. Chem. Eng.*, 2020, **5**, 2250–2259.
7 D. Cambié and T. Noël, *Top. Curr. Chem.*, 2018, **376**(6), 45.
8 M. Pasha, S. Liu, M. Shang, M. Qiu and Y. Su, *Chem. Eng. J.*, 2022, **445**, 136663.
9 D. Cambié, C. Bottecchia, N. J. W. Straathof, V. Hessel and T. Noël, *Chem. Rev.*, 2016, **116**(17), 10276–10341.
10 M. Jacobs, G. Meir, A. Hakki, L. C. J. Thomassen, S. Kuhn and M. E. Leblebici, *Chem. Eng. Process.*, 2022, **181**, 109138.
11 W. Wang, M. Li and C. Xu, *Ind. Eng. Chem. Res.*, 2024, **63**(5), 2374–2383.
12 A. A. Miskevich and V. A. Loiko, *J. Exp. Theor. Phys.*, 2011, **113**(1), 1–13.
13 M. I. Mishchenko, L. D. Travis and A. A. Lacis, *Multiple Scattering of Light by Particles*, Cambridge University Press, New York, 2006.
14 V. A. Loiko and A. A. Miskevich, in *Springer Series in Light Scattering*, ed. A. Kokhanovsky, Springer, Cham, 2018, vol. 2, pp. 101–230.
15 L. Buglioni, F. Raymenants, A. Slattery, S. D. A. Zondag and T. Noël, *Chem. Rev.*, 2022, **122**(2), 2752–2906.
16 J. P. Knowles, L. D. Elliott and K. I. Booker-Milburn, *Beilstein J. Org. Chem.*, 2012, **8**, 2025–2052.
17 M. Berton, J. M. de Souza, I. Abdiaj, D. T. McQuade and D. R. Snead, *J. Flow Chem.*, 2020, **10**(1), 73–92.
18 M. Torbacke and Å. C. Rasmuson, *AIChE J.*, 2004, **50**(12), 3107–3119.
19 M. Zheng, J. Liu, L. Tian, Z. Yan, C. Zhou, H. Li, C. Zheng, J. Chen and H. Zheng, *Powder Technol.*, 2024, **434**, 119292.
20 Z. Dong, S. D. A. Zondag, M. Schmid, Z. Wen and T. Noël, *Chem. Eng. J.*, 2022, **428**, 130968.
21 A. Valotta, L. Malihan-Yap, K. Hinteregger, R. Kourist and H. Gruber-Woelfler, *ChemSusChem*, 2022, **15**(22), e202201468.
22 K. S. Elvira, X. C. i Solvas, R. C. R. Wootton and A. J. deMello, *Nat. Chem.*, 2013, **5**(11), 905–915.
23 X. Duan, Z. Huang, G. Qian, K. He, J. Zhang, L. Mleczko and X. Zhou, *Chem. Eng. Sci.*, 2020, **213**, 115397.
24 M. Atobe, *Curr. Opin. Electrochem.*, 2017, **2**(1), 1–6.
25 X. Sheng, Y. Zheng, W. Li, R. Gao, L. Du and Y. Wang, *Chem. Eng. Sci.*, 2020, **226**, 115862.
26 J. Liu, P. Wang, N. Zhao, Z. Xu and X. Huang, *Chem. Eng. J.*, 2023, **468**, 143843.
27 C. Pratley, Y. Shaalan, L. Boulton, C. Jamieson, J. A. Murphy and L. J. Edwards, *Org. Process Res. Dev.*, 2023, **28**(5), 1725–1733.
28 H. E. Bonfield, T. Knauber, F. Lévesque, E. G. Moschetta, F. Susanne and L. J. Edwards, *Nat. Commun.*, 2020, **11**(1), 804.
29 M. J. Nieves-Remacha, A. A. Kulkarni and K. F. Jensen, *Ind. Eng. Chem. Res.*, 2013, **52**(26), 8996–9010.
30 S. Zhao, Y. Wei, P. Yu, F. Yuan, C. Li, Q. Gao, L. Sheng, Y. Feng, J. Yang, W. He, N. Zhu, Y. Li, D. Ji and K. Guo, *J. Ind. Eng. Chem.*, 2024, **133**, 207–218.
31 S. Zhao, L. Sheng, W. He, N. Zhu, Y. Li, D. Ji and K. Guo, *J. Chem. Technol. Biotechnol.*, 2022, **97**(11), 3121–3131.
32 H. S. Santana, D. S. Tortola, J. L. Silva Jr and O. P. Taranto, *Energy Convers. Manage.*, 2017, **141**, 28–39.
33 L. Wang, Q. Wang, R. Zhao, Y. Tao, K.-Z. Ying and X.-Z. Mao, *ACS Sustainable Chem. Eng.*, 2021, **9**(4), 1550–1558.
34 S. Kumar, D. Jia, A. A. Kubar, X. Zou, Z. Huang, M. Rao, C. Kuang, J. Ye, C. Chen, F. Chu and J. Cheng, *Ind. Eng. Chem. Res.*, 2022, **61**(38), 14181–14188.
35 A. A. Kubar, J. Cheng, S. Kumar, S. Liu, S. Chen and J. Tian, *Bioresour. Technol.*, 2021, **320**, 124337.
36 G. Plantard, R.-P. Brice, S. Anastasia, K. Somar, L. G. L. Corinne, W. Karine, E. Ribeiro and G. Vincent, *Chem. Eng. Sci.*, 2024, **285**, 119470.
37 H. Shi, K. Nie, B. Dong, L. Chao, F. Gao, M. Ma, M. Long and Z. Liu, *Chem. Eng. J.*, 2020, **392**, 123642.
38 S. Mu, Y. Lu and G. Zhu, *Chem. Eng. J.*, 2024, **480**, 147967.
39 E. Bennour, N. Kaid and A. Mouissi, *Ind. Eng. Chem. Res.*, 2024, **63**(6), 2861–2874.
40 X. Qi, J. Wang, C. Chen and L. Wang, *Chem. Eng. Process.*, 2024, **196**, 109677.
41 Y. Zhang and X. Chen, *J. Dispersion Sci. Technol.*, 2022, **43**(3), 439–445.
42 W. Yang, S. Feng, X. Zhang, Y. Wang, C. Li, L. Zhang, J. Zhao, G. G. Gurzadyan and S. Tao, *ACS Appl. Mater. Interfaces*, 2021, **13**(32), 38722–38731.
43 X. Wang, Z. Liu, B. Wang, Y. Cai and Q. Song, *Anal. Chim. Acta*, 2023, **1279**, 341685.
44 J. P. B. Howell, D. R. Mott, J. P. Golden and F. S. Ligler, *Lab Chip*, 2004, **4**(6), 663–669.

45 A. Qamareen, M. A. Ansari and S. S. Alam, *Chem. Eng. Process.*, 2022, **176**, 108945.
46 H. Xue and J. Jin, *Ind. Eng. Chem. Res.*, 2024, **63**(3), 1680–1689.
47 S. Yuan, B. Jiang, T. Peng, M. Zhou and D. Drummer, *Chem. Eng. Process.*, 2022, **171**, 108747.
48 C. K. Chung, T. R. Shih, C. K. Chang, C. W. Lai and B. H. Wu, *Chem. Eng. J.*, 2011, **168**(2), 790–798.
49 C. Hou, L. Li, R. Lv, Z. Tian and X. Chen, *Chem. Eng. Technol.*, 2021, **44**(12), 2220–2227.
50 X. Wang, Z. Liu, Y. Cai, B. Wang and X. Luo, *Anal. Chim. Acta*, 2021, **1155**, 338355.
51 J. J. Chen, C. H. Chen and S. R. Shie, *Int. J. Mol. Sci.*, 2011, **12**(6), 3500–3524.
52 K. Loubière, M. Oelgemöllerc, T. Aillet, O. Dechy-Cabaret and L. Prat, *Chem. Eng. Process.*, 2016, **104**, 120–132.
53 E. Kayahan, M. Jacobs, L. Braeken, L. C. J. Thomassen, S. Kuhn, T. van Gerven and M. E. Leblebici, *Beilstein J. Org. Chem.*, 2020, **16**, 2484–2504.
54 Y. Su, N. J. W. Straathof, V. Hessel and T. Noël, *Chem. – Eur. J.*, 2014, **20**(34), 10562–10589.
55 S. Guo, L. Zhan and B. Li, *Chem. Eng. J.*, 2023, **477**, 147011.
56 X. Wang, T. Zhang, L. Lv, W. Tang, R. K. Gupta and S. Tang, *Ind. Eng. Chem. Res.*, 2022, **61**(25), 9122–9135.
57 G. J. Janz and S. C. Wait Jr, *J. Chem. Phys.*, 1955, **23**, 1550–1551.
58 T. Claes, A. Dilissen, M. E. Leblebici and T. V. Gerven, *Chem. Eng. J.*, 2019, **361**, 725–735.
59 M. E. Leblebici, G. D. Stefanidis and T. V. Gerven, *Chem. Eng. Process.*, 2015, **97**, 106–111.
60 F. Li, P. Cheng, X. Li, Y. Zou and S. Tao, *Ind. Eng. Chem. Res.*, 2024, **63**(42), 17734–17743.